www.lajss.org
Latin American Journal of Solids and Structures 2 (2005) 195–217

Multiple barrelling in axial compression of cylindrical tubes

P. K. Gupta[a] and N. K. Gupta[b,*]

[a]Civil Engineering Group, Birla Institute of Technology and Science Pilani, 333031, India
[b]Department of Applied Mechanics, Indian Institute of Technology Delhi, New Delhi, 110016, India

Abstract

Quasi-static axial compression tests were conducted on aluminium round tubes of different diameter to thickness (D/h) ratios. All the tested tubes deformed in axisymmetric mode. However those having D/h ratio less than around 8 collapsed in multiple barrelling while others in concertina mode. The present paper specifically deals with the development of, axisymmetric multiple barrelling mode of collapse while concertina mode of collapse is presented in our previous paper [4]. The compression process was also numerically modelled using non-linear finite element code FORGE2 [3]. The tube material was modeled as rigid-viscoplastic. A computational model of compression process is presented. Experimental and computed load-compression and energy-compression curves and deformed shapes of the tubes are compared. Predicted variations of equivalent strain, equivalent stress and different components of strain rate and stress tensors are presented and discussed. Effect of friction present between tube-platen interfaces on the development of mode of collapse is also presented and discussed. On the basis of the experimental and computational findings mechanics of multiple barrelling is discussed.

Keywords: axial compression, round tubes, axisymmetric multiple barrelling, FORGE2.

1 Introduction

Metallic tubes are commonly used as energy absorbing devices. They deform plastically in several different modes, each of which has associated energy dissipation. The tubular elements in energy absorbers can be configured in various ways so that when an impact does occur, they deform axially, laterally or in some combination. Plastic collapse of thin-walled shells of various shapes, sizes and materials under different loading conditions has been studied in the past [1,2,4,5,7,8]. The important characteristics of the energy absorbers, their selection criteria and various modes of plastic deformation of thin-walled shells such as splitting, tube inversion and folding are discussed in [2]. Johnson and Reid [7] reviewed the modes of deformation of various thin-walled shells and their corresponding load-compression graphs. They also discussed factors influencing the modes of collapse of structural components in dynamic loading.

*Corresponding author (narinder_gupta@yahoo.com) Received 6 July 2005; In revised form 11 July 2005

Notations

$\tilde{S}_{ij}$	Deviatoric stress tensor
K	Material consistency
$\dot{\bar{\varepsilon}}$	Effective strain rate
m	Strain rate sensitivity index
K_0	Constant term
a	Strain hardening term
$\bar{\varepsilon}$	Effective strain
$\bar{\sigma}$	Effective stress
β	Temperature sensitivity term
T	Temperature in absolute value
τ	Shearing stress
α	Friction coefficient, α_1 and α_2 at top and bottom
p	Sensitivity to sliding velocity
ΔV	Relative sliding velocity between tube and platen
$d\Omega$	Contact surface between platen and tube
D	Mean diameter of tube in mm.
h	Thickness of tube in mm
δ	Compression or platen displacement

Study of the axisymmetric concertina mode of collapse has been carried out by researchers in the past by performing experiments and proposing analytical models. Recently finite element method has also been employed [1,4,8] to analyse the axisymmetric concertina mode of collapse. However available literature is scare regarding the study of axisymmetric multiple barrelling mode of collapse.

The present study is devoted to experimental and finite element analysis of the axial compression of thick round aluminium tubes under quasi-static loading. Although the tubes can deform both in axisymmetric concertina and axisymmetric multiple barrelling modes of collapse due to their lower D/h ratios the focus of this paper is on the axisymmetric multiple barrelling mode. Experimental and computed load-compression & energy-compression curves as well as deformed shapes at different stages of compression are presented. A numerical study was also carried out to investigate the effect of friction present between the tube-platen interfaces on the axisymmetric multiple barrelling mode of collapse. Mechanics of the development of axisymmetric multiple barrelling mode of collapse is investigated and discussed.

2 Experimental work

Aluminium round tubes of average diameter to thickness ratio ranging from 6 to 38 were axially compressed between two rigid platens in as-received condition under quasi-static loading on an INSTRON machine (model 1197) of 50 T capacity at cross head speed of 10 mm/minute. The length of specimens was taken equal to twice their outer diameter. Load-compression

curves were recorded on the automatic chart recorder of the machine. The deformed shapes at different stages of compression were recorded. The compression of the specimens which deform in concertina mode of collapse was carried out till formation of one complete fold, while the specimens which deform in axisymmetric multiple barrelling compressed till 40% to 65% of their initial height. Repeatability of the results was ensured by repeating the experiments on at least three identical specimens. It was found that all the tubes having D/h ratio less than around 8 were collapsed, in axisymmetric multiple barrelling while others (having D/h ratio greater than 8 but less than 38) in axisymmetric concertina mode. Fig. 1 shows a typical axisymmetric multiple barrelling and concertina mode of collapse of tested tubes having different D/h values.

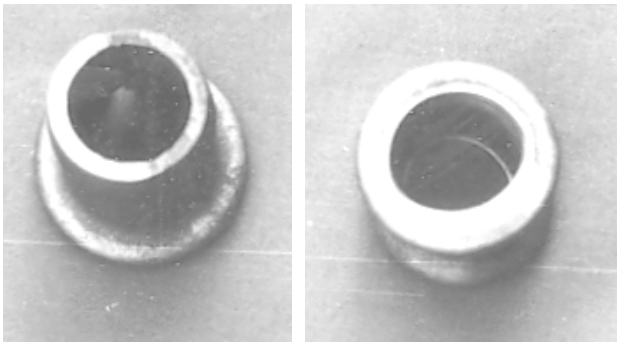

(a) (b)

Figure 1: True deformed shapes of the axisymmetric (a) concertina and (b) multiple barreling mode of collapse.

3 Computational work

3.1 Constitutive equations

The material of the deforming tube is assumed as homogeneous, isotropic, incompressible and rigid visco-plastic. The constitutive relation for such a material is given by the so-called Norton-Hoff law [6] as follows;

$$\begin{gathered} \tilde{S}_{ij} = 2K \left(\sqrt{3}\,\dot{\bar{\varepsilon}}\right)^{m-1} \tilde{\dot{\varepsilon}}_{ij}, \\ \text{where } \dot{\bar{\varepsilon}} = \left(\frac{2}{3}\,\tilde{\dot{\varepsilon}}_{ij} \cdot \tilde{\dot{\varepsilon}}_{ij}\right)^{\frac{1}{2}}, \; \tilde{\dot{\varepsilon}}_{ij} = \frac{1}{2}\left(v_{i,j} + v_{j,i}\right) \end{gathered} \tag{1}$$

where $\tilde{S}_{ij}$, $\tilde{\dot{\varepsilon}}_{ij}$, K and m represent the components of the deviatoric stress tensor, strain rate tensor, material consistency and strain rate sensitivity index respectively. The v_i is the component of velocity in the direction "i" at any point of the problem domain. The incompressibility

condition is written as below

$$\text{div } \tilde{v} = 0 \text{ over the problem domain} \tag{2}$$

where $\tilde{v}$ is the velocity vector at any point of the domain. The material consistency K depends upon the thermo-mechanical condition of the material. For most metals, the behaviour of K can be approximated by means of the following multiplicative law;

$$\mathrm{K} = \mathrm{K_o}\,(1 + a\bar{\varepsilon})\ \mathrm{e}^{\beta/T} \tag{3}$$

where K_0 is a constant, a is the strain hardening parameter, β is the temperature sensitivity term and T is the absolute temperature. The values of the parameters K_0, a , and m can be found by conducting uniaxial tensile tests at different strain rates and temperatures. By suitable choice of these parameters, equations (1) and (3) can approximate the mechanical behaviour of most of the metals at different temperature and strain rate ranges. Using above equations the constitutive equation for uniaxial case gets the form as follows

$$\bar{\sigma} = K_{ot}\,(1 + a\bar{\varepsilon})\,\dot{\bar{\varepsilon}}^{m} \tag{4}$$

where $\bar{\sigma}$ is the equivalent stress for uniaxial case and $K_{ot} = K_o\left(\sqrt{3}\right)^{m+1} e^{\beta/T}$

The friction between the workpiece and the tool is modeled with a viscoplastic law

$$\tau = -\alpha K\,|\Delta V|^{p-1}\,\Delta V \text{ on } S_f \tag{5}$$

where α is the coefficient of friction, ΔV is the relative sliding velocity, p is a constant and S_f denotes the frictional surface. To perform the simulation of the deformation process of each tube specimen by FORGE2 [3] code some material property parameters which are strain hardening coefficient (a), strain rate sensitivity index (m) and consistency of material (K_o) are required as input. Hence tension tests were performed at three different strain rates to determine these material property parameters. To perform tension tests, six tension test specimens were prepared from each tube.

3.2 Determination of material properties parameters

The following constitutive relation models the mechanical behaviour of the tube material

$$\bar{\sigma} = K_{ot}\,(1 + a\bar{\varepsilon})\,\dot{\bar{\varepsilon}}^{m} \tag{6}$$

where, $K_{ot} = K_o\left(\sqrt{3}\right)^{m+1} e^{\beta/T}$, and $\bar{\sigma}$ is the effective stress, K_0 is a constant, a is the strain hardening parameter, m is strain rate sensitivity index, β is the temperature sensitivity term and T is the absolute temperature. If the compression process is performed at a more or less constant temperature then the value of $e^{\beta/T}$ remains same at all points of the deforming body. To determine the above material parameters namely K_o, a, and m uniaxial tensile tests were

conducted at three different strain rates. Special tensile test specimens were prepared by cutting the same tubes from their axial direction as were used for carrying out the compression tests. A universal testing machine (MTS model no. 810 of 250 kN capacity) was used to carry out the tests. Load-extension curves were recorded using the chart recorder of the machine. The true stress versus true strain curves were calculated and plotted from the recorded load-extension curves. These true stress versus true strain curves were used to calculate the material properties of tube specimens. These material parameters for different tube specimens are presented in Table 1 in S. I. system.

Specimen	Average diameter D (mm)	Thickness h (mm)	D/h	Material properties		
				K_0 (MPa)	a	m
A254	25.00	4.01	6.25	141.5	1.142	.00154
A253	21.93	3.03	7.23	140.5	1.122	.00134
A252	23.06	2.04	11.30	136.2	1.758	.012
A251	24.27	1.03	23.56	111.3	2.38	.00154
A383	34.73	3.13	11.09	142.2	1.34	.126
A381	36.93	1.03	35.85	134.8	2.8	.0012
A503	47.66	3.44	13.85	138.5	1.91	.00341
A502	48.92	1.68	29.12	143.5	1.915	.00021
A501	48.7	1.3	37.46	146.2	1.91	.000171
A802	79.2	2.18	36.33	89.36	0.61	.00011

Table 1: Dimensions and material properties of specimens.

3.3 Computational model and its features

In the finite element model of the compression process the top platen was modeled to move on its axis with a downward velocity of 10 mm/minute while the bottom platen as stationary. The contact between the platen and tube surfaces has been assumed as sliding unilateral [3]. Friction factor at the platen tube interface is assumed to be given and equal to $\alpha_1 = 0.45$, $\alpha_2 = 0.15$ [4]. Since the original and experimentally deformed tubes were axisymmetric so a axisymmetric Finite Element model of the compression process is proposed and presented. Fig. 2 shows the computational model used for the present investigation.

Six noded isoparametric triangular elements have been used to discretize the tube domain. The temperature is kept constant and equal to room temperature 310° K. Compression process of each tube specimen was simulated using FORGE2 code and analyzed. The total deformation of the specimen was carried out into small steps called as increments. The value of the incremental strain in each increment was taken equal to 1% of the current tube height. Number of elements used for discretization of the problem domain were varied between 400 to 628. CPU time required for completion of the simulations was between 1300 to 1600 s. on a SUN workstation.

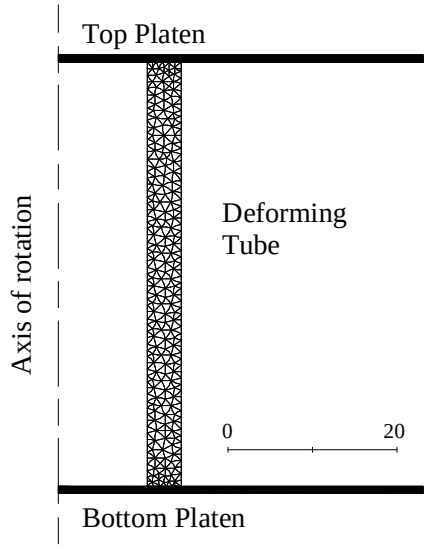

Figure 2: Axisymmetric two dimensional Computational Model.

Number of remeshings required to finish the compression of different specimens were between three to eleven. The computer memory required to store the results of these simulations varied from 10 to 15 MB.

4 Results and discussions

4.1 Verification of computational model

To verify the proposed Finite Element model presented for study of development of axisymmetric multiple barrelling mode of collapse experimental and computed load-compression and energy-compression curves as well as deformed shapes at different stages of compression process were compared for specimens A254 and A253. Fig. 3 shows typical computed deformed profiles at various stages of compression for specimen A254. Fig. 4 presents the comparison of experimental and computed load-compression curves for specimens A254 and A253. For both the specimens the load in the load-compression curve increases continuously throughout the compression process. Fig. 5 depicts the corresponding energy-compression curves for both specimens. Comparison of experimental and computed deformed profiles at various stages of development of multiple barrelling mode of collapse for both specimens A254 and A253 is presented in Table 2 by comparing the coordinates of key points a1, b1, c1 marked in Fig. 6. After seeing the Fig. 4 and Fig. 5 one can say that the computed load-compression and enery-compression variations have good aggrement with the experimental ones. The computed and true deformed shapes are also match quite well (see Table 2).

Compression of tube (mm)	Coordinate X, Y of key points in mm					
	Point "a1"		Point "b1"		Point "c1"	
	Exp.	Comp.	Exp.	Comp.	Exp.	Comp.
9.8	16.5, 29.7	16.73, 29.81	15.9, 16.23	15.75, 21.32	16.3, 10.5	16.41, 10.72
19.0	19.2, 23.2	19.04, 23.41	13.1, 14.13	16.69, 16.5	18.5, 8.6	18.38, 8.33
23.5	19.6, 20.1	19.98, 20.34	13.6, 14.02	17.05, 14.07	19.1, 7.3	19.23, 7.12
30.0	20.6, 15.6	20.93, 15.46	12.8, 13.06	17.24, 10.03	20.3, 5.3	20.46, 5.14

(a) Specimen A254

Compression of tube (mm)	Coordinate X, Y of key points in mm					
	Point "a1"		Point "b1"		Point "c1"	
	Exp.	Comp.	Exp.	Comp.	Exp.	Comp.
17.17	16.3, 24.9	16.4, 24.95	11.9, 16.2	13.66, 16.49	14.1, 7.2	16.03, 7.46
21.14	16.8, 22.1	17.32, 22.13	12.1, 14.1	13.81, 14.34	14.1, 6.7	16.67, 6.82
23.11	17.1, 20.7	17.72, 20.88	12.6, 14.0	13.91, 14.12	14.2, 6.2	16.91, 6.25
23.74	17.2, 20.2	17.82, 20.43	12.7, 13.0	13.93, 13.32	14.2, 6.1	17.00, 6.13
25.20	17.4, 18.9	18.01, 19.10	12.8, 12.9	13.95, 13.06	14.3, 5.6	17.24, 5.75

(b) Specimen A253

(Exp.- Experimental, Comp.- Computational)

Table 2: (a-b) Comparison of experimental and computed deformed profiles.

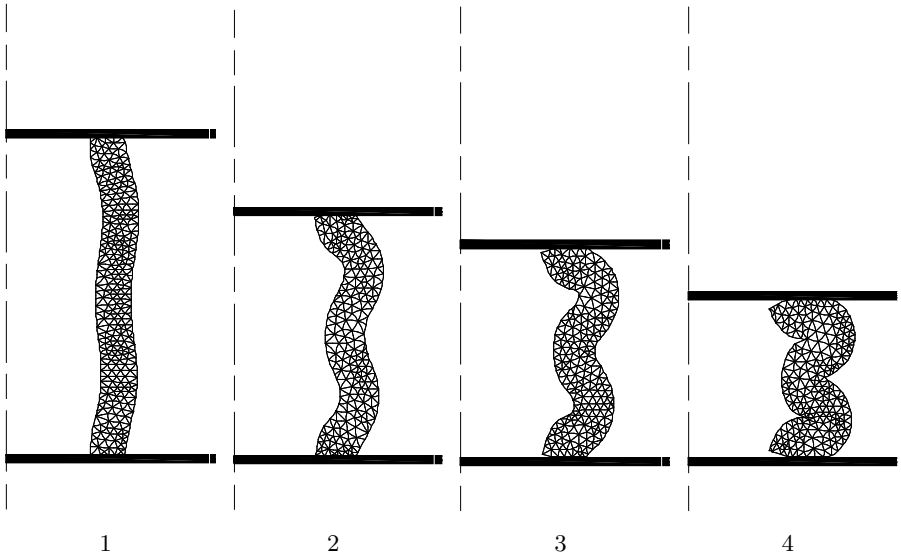

Figure 3: Computed deformed profiles after (1) 9.77, (2) 19.01, (3) 23.5, and (4) 30.0 mm of compression (specimen A254, $\alpha_1 = 0.45$, $\alpha_2 = 0.15$).

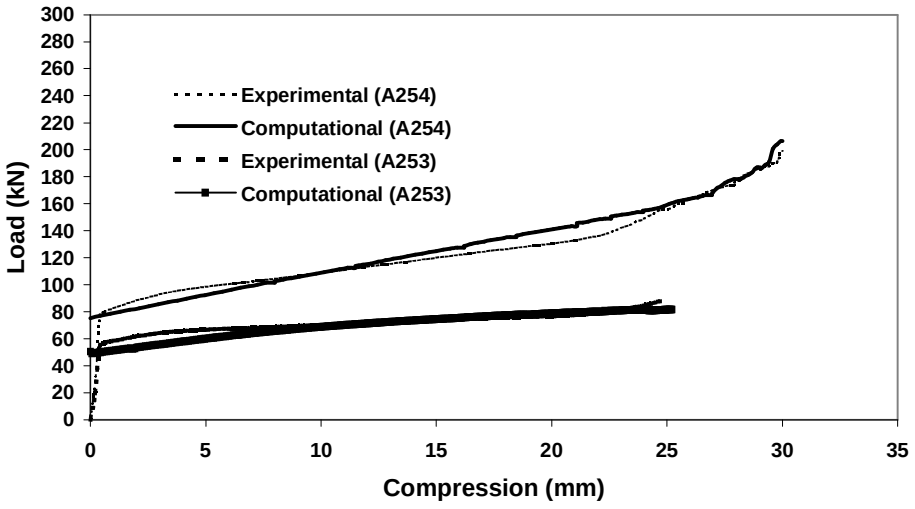

Figure 4: Comparison of experimental and computed load-compression curves.

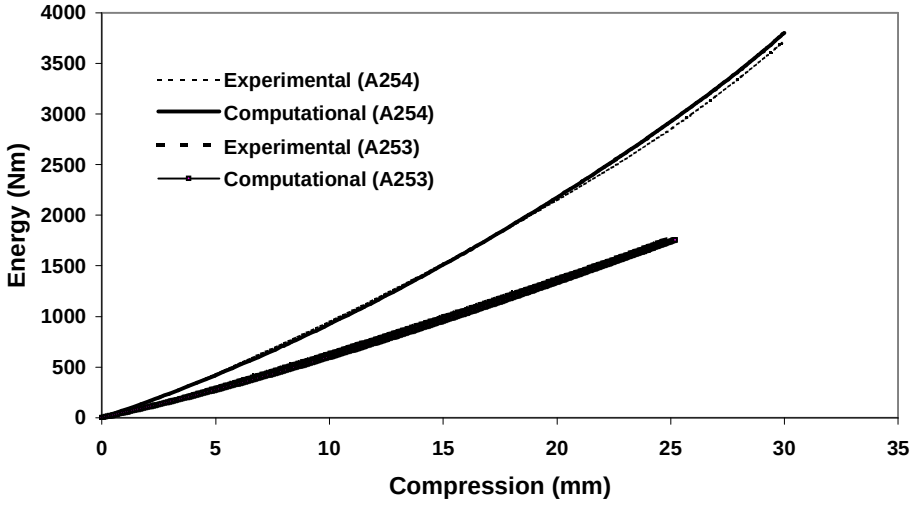

Figure 5: Comparison of experimental and computed energy-compression curves.

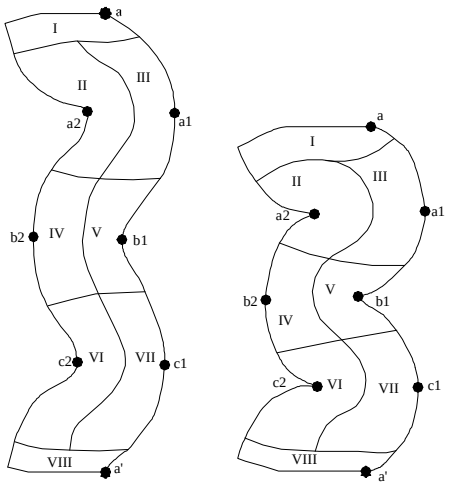

(I) $\delta_1 = 23.5$ mm (II) $\delta_2 = 30$ mm

Figure 6: Demarcation of zones and points of interest at two stages in the deforming tube.

4.2 Typical computational results

To understand the compression process of the thick tubes which were collapsed in axisymmetric multiple barrelling mode, variations of the nodal velocity, equivalent strain rate, equivalent strain, equivalent stress and different components of strain rate, stress and strain have been studied. For this purpose the results of a particular tube, which has been used as a typical case are as follows:

average diameter of tube (D)	25.0 mm
tube thickness (h)	4.01 mm
D/h	6.25
material constant showing consistency K_0	141.5 MPa
strain rate sensitivity (m)	0.0154
strain-hardening parameter (a)	1.142
α_1	0.45
α_2	0.15
Number of elements and nodes used to discretize the domain	628 and 1409 respectively
Strain increased in each increment	1%
Number of remeshings required to complete the compression process	9
CPU time required	1509 seconds

To carried out simulation until 30 mm compression the required number of increments were 117. Results at two typical stages of compression are presented. These stages are at (I) 23.5 mm (at increment number 80), and (II) 30 mm (at increment number 117) of platen displacements.

The tube section has been demarcated into eight different zones and eight locations a1, a2, b1, b2, c1, c2, a and a$'$ in these eight zones are identified as given below (Fig. 6).

- Zone I and VIII: These zones are adjoining the interfaces of the specimen with the top and bottom platen.
- Zone II, V and VI: These are the zones where compressive stresses are developed during the compression.
- Zone III, IV and VII: Zones where tensile stresses are set-up due to barrelling.

Velocity distribution. The distribution of resultant flow velocity and its direction are shown in Figs. 7(a) and 7(b). During the whole compression process, relatively high values of velocity occur in zones II, III, IV and V adjoining the moving platen. Flow velocities at the points in the lower part of the tube specimen have relatively low magnitudes due to their nearness to the

stationary platen. The flow pattern indicates that the whole tube deforms simultaneously no part of the tube remains idle. This is what actually happens in the experiments.

Strain rate components. The variation of strain rate components $\dot{\varepsilon}_{rr}$, $\dot{\varepsilon}_{zz}$, $\dot{\varepsilon}_{rz}$ and $\dot{\varepsilon}_{\theta\theta}$ are shown in Figs. 7(c), 7(d), 7(e) and 7(f) respectively.

The strain rate component $\dot{\varepsilon}_{rr}$ has higher value contours in the zones I, II, V, VI and VIII upto 23.5 mm compression. As the compression process proceeds the higher value contours get concentrate in zone V only and specifically around point b1. At 30 mm compression lower value contours concrentrate around point c2.

Strain rate component $\dot{\varepsilon}_{zz}$ has higher absolute values in the compression zones, namely II, V and VI (Fig. 6) during the compression process.

Fig 7(e) depicts the variation of strain rate component $\dot{\varepsilon}_{rz}$. The distribution shows interesting results. Contours appear to be quite symmetrical about lines aa2, a2b1, b1c2, c2a$'$ (see Fig. 6). The concentration of contours in certain regions indicates the occurrence of shearing in those places.

The strain rate component $\dot{\varepsilon}_{\theta\theta}$ is positive in the regions marked as II, III, V, VI and VII (Fig. 6) The radius of tube in these regions is found to increase during the compression process. The $\dot{\varepsilon}_{\theta\theta}$ in zones IV is tensile in character and lower in magnitude because the radius of this section increases but with less amount as compared to the zones II, III, VI and VII (Fig. 6). The compressive strain rates are higher in zones I and VIII because tube material in these zones displaces towards the axis of the tube.

Equivalent strain rate. Fig. 7(g) shows the distribution of equivalent strain rate $\dot{\bar{\varepsilon}}$ (EbP) at different milestones. Concentration of higher value contours in a region depicts current region of deformation. The contours are co-centric about points a, a$'$ a2, b1 and c2 (Fig. 6) The maximum value of equivalent strain rate occurs at point a2 at 23.5 mm compression while at c2 at 30 mm compression. The higher values occur in the compression zones of the deformed tube.

Components of stresses. The variations of different stress components σ_{rr}, σ_{zz}, σ_{rz} and $\sigma_{\theta\theta}$ are depicted in Figs. 7(h), 7(i), 7(j) and 7(k) respectively.

The distribution of stress component σ_{rr} shows that its minimum value occurs in the zones I and VIII at the platen tube interface. The distribution in remaining part of the tube is in such a way that the higher and lower values occur in tension and compression zones respectively.

The distribution of stress components σ_{zz} shows that the magnitude of the maximum tensile stress is less than half of the maximum value of compressive stress during the whole compression process. This indicates that the tube is under axial compression and bending.

The distribution of shear stress component σ_{rz} appears to be quite symmetrical about two orthogonal planes marked at different locations as shown in Fig. 6.

The distribution of stress component $\sigma_{\theta\theta}$ shows hoop tension in the tension zones namely III, IV and VII while hoop compression in the compression zones II, V and VI of the specimen.

Principal stress. Fig. 7(l) shows the distribution of principal stress. Upto 23.5 mm compression maximum tensile principal stress is equal to 530.4 Mpa and it occurs around point a2. After comparing the variation with contours of $\sigma_{\theta\theta}$ it is found that $\sigma_{\theta\theta}$ is the maximum

tensile principal stress. At 30 mm compression maximum tensile stress occurs around point c2 and equal to 721.8 Mpa.

Equivalent strain. Fig. 7(m) depicts the variation of equivalent strain $\dot{\bar{\varepsilon}}$ (Eb) at two stages of compression. The higher values of equivalent strain occur at points a2, b1, c2, a and a′ (see Fig. 6) during the whole compression process. Upto 23.5 mm compression the highest value of equivalent strain occurs at a2 while at 30 mm compression the highest value of the equivalent strain shifted to the point c2. The point c2 is also the seat of the largest change in curvature. The change in magnitude of contours is rapid in zone I, VIII, II, VI in the vicinity of points a, a′ and b2, a2. The contours appear to-be co-centric about these points.

Equivalent stress. Fig. 7(n) shows the variation of the equivalent stress $\bar{\sigma}$ (Seq). The variation is quite similar to the equivalent strain. The highest value of it is 944.2 MPa during the compression process. The values of the equivalent stress at points a, a′ a2, b1 and c2 (see Fig. 6) are more than 450 Mpa at both the stages of compression.

4.2.1 Development of strains and stresses

To understand the compression process the variations of the equivalent strain and equivalent stress were studied after 23.5 mm and 30 mm compressions on the boundary of the deforming tube (see Figs. 8(a-b)). The key points a, a′, a1, a2, b1, b2, c1 and c2 were approximately located in the graphs. The approximate values of the equivalent strain $\dot{\bar{\varepsilon}}$ at points a, a′, a1, a2, b1, b2, c1 and c2 were 1.4, 0.51, 0.3, 0.4, 1.15, 0.17, 0.33 and 1.34 respectively after 23.5 mm compression. The corresponding approximate values after 30 mm compression were 1.6, 0.75, 0.41, 0.96, 2.1, 0.2,0.41 and 2.59.

The approximate values of the equivalent stress $\bar{\sigma}$ at points a, a′, a1, a2, b1, b2, c1 and c2 were found to be 632, 386, 335, 436, 567, 296, 249 and 621 MPa respectively after 23.5 mm compression. The corresponding approximate values after 30 mm compression were 682, 453, 359, 509, 824, 291, 257 and 944 MPa. The equivalent strain was very small in magnitude near to zero at some points throughout the comprtession process. These points are located on the boundary between points a & a2 and c2 & a′ in the zone I & VIII. This shows that during the compression process except some small regions in zone I and VIII, whole tube deforms with major deformation concentrated around the discussed eight key points (see Fig. 6).

It is clear now that the major deformation occurs in the tube around the eight key points. To clearly understand the compression process the history of deformation of the six key points a1, a2, b1, b2, c1 and c2 were collected during the compression process. Since points a and a' fall on the tube-platen interface so their history of deformation was not further investigated.

Fig. 9(a-c) presents the variation of equivalent strain ($\bar{\varepsilon}$), $\dot{\varepsilon}_{zz}$ and hoop strain ($\dot{\varepsilon}_{\theta\theta}$) at all these six points during the compression process. It is clear from the Fig. 9(a) that at all points the magnitue of the $\bar{\varepsilon}$ increases throughout the compression process but with high rates at points a2, b1 and c2 while with slow rates at points a1, b2 and c1. Consequently the magnitude of $\bar{\varepsilon}$ at points a1, b2 and c1 are very small as compared to at the points a2, b1 and c2 after 30

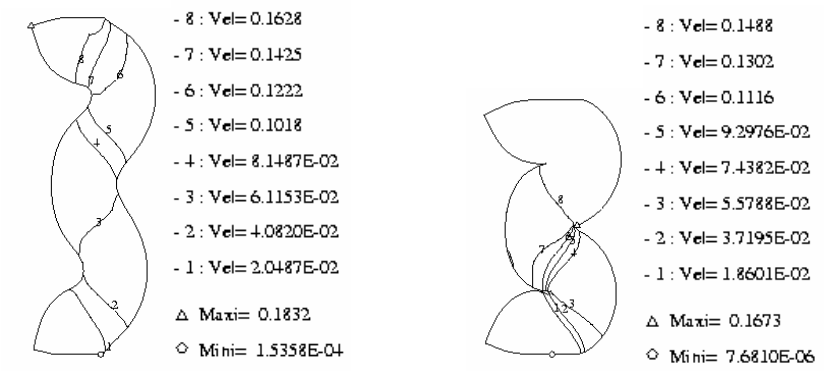

(a) Magnitude of nodal velocity

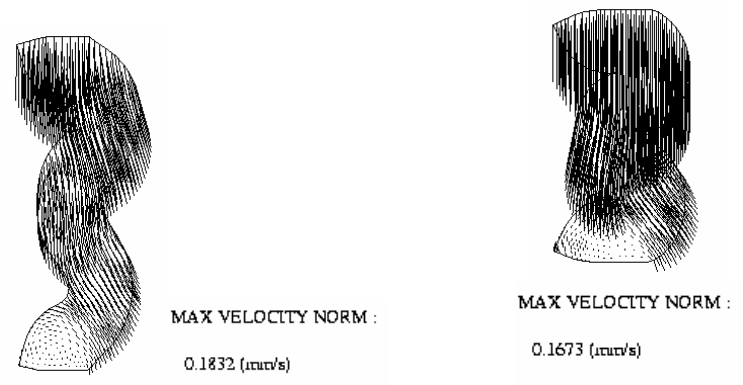

(b) Direction of nodal velocity

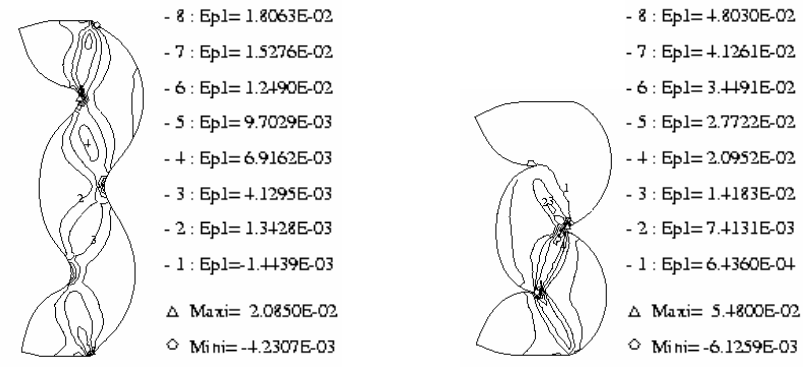

(c) Strain rate $\dot{\varepsilon}_{rr}$

(continue)

Figure 7: Predicted variation of nodal velocity, equivalent strain, different strain rates, and stresses at two stages (I) δ_1 =23.5 mm, and (II) δ_2 = 30 mm compression (specimen A254).

(continued)

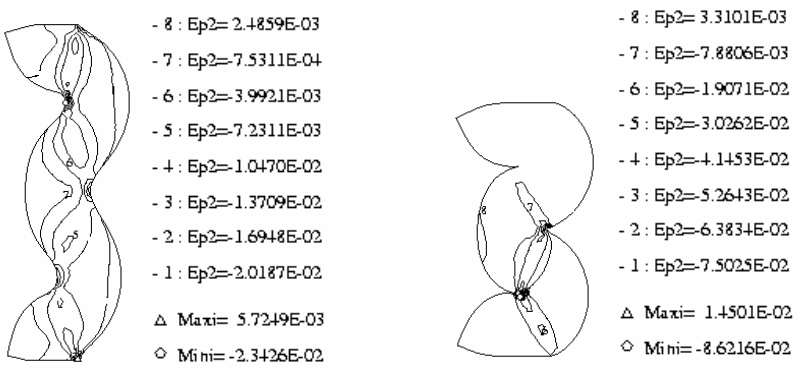

(d) Strain rate $\dot{\varepsilon}_{zz}$

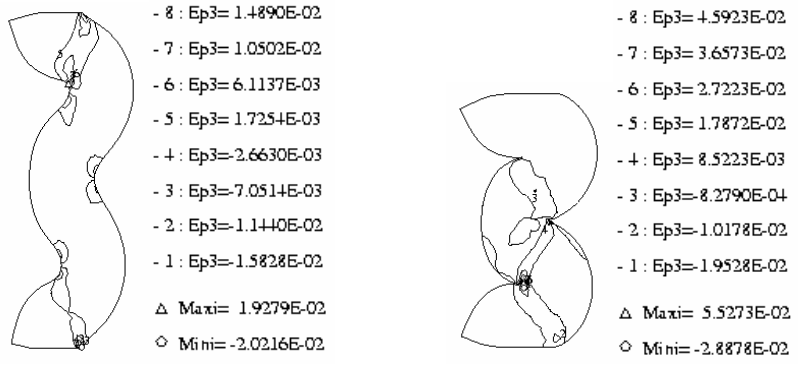

(e) Strain rate $\dot{\varepsilon}_{rz}$



(f) Strain rate $\dot{\varepsilon}_{\theta\theta}$

(continue)

Figure 7: Predicted variation of nodal velocity, equivalent strain, different strain rates, and stresses at two stages (I) δ_1 =23.5 mm, and (II) δ_2 = 30 mm compression (specimen A254).

(continued)

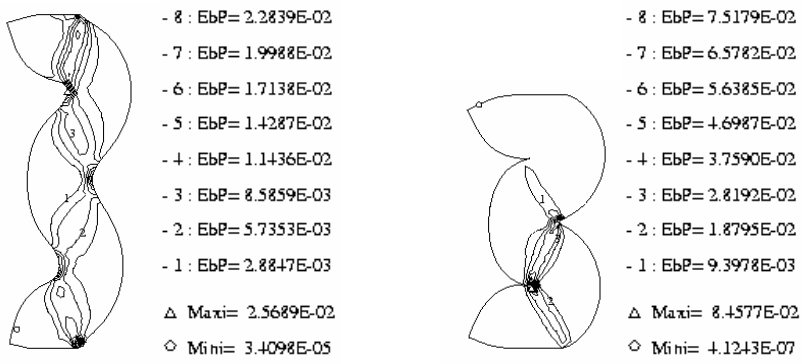

(g) Equivalent strain rate $\dot{\bar{\varepsilon}}$

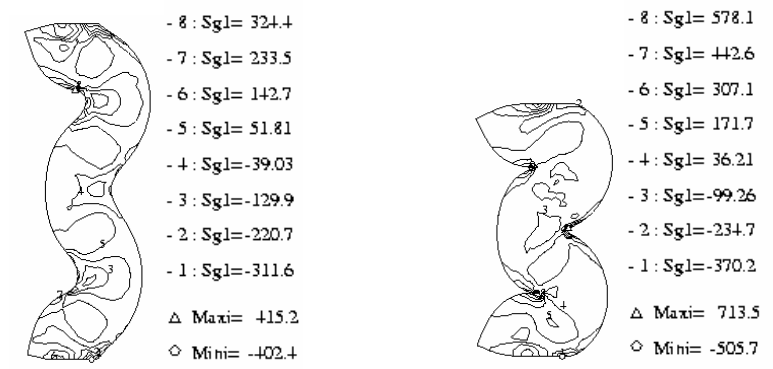

(h) Strain rate σ_{rr}

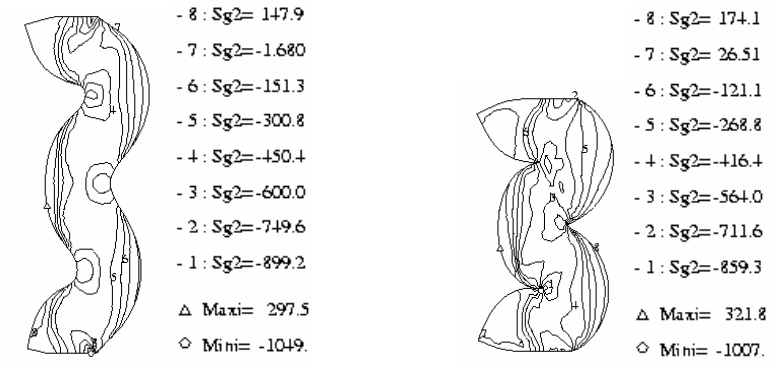

(i) Stress σ_{zz}

(continue)

Figure 7: Predicted variation of nodal velocity, equivalent strain, different strain rates, and stresses at two stages (I) δ_1 =23.5 mm, and (II) δ_2 = 30 mm compression (specimen A254).

(continued)

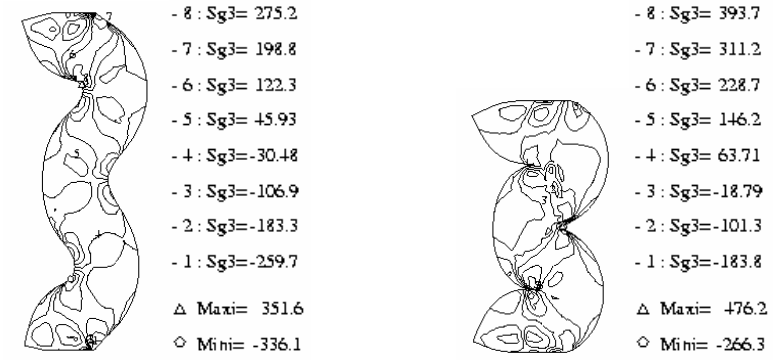

(j) Stress σ_{rz}

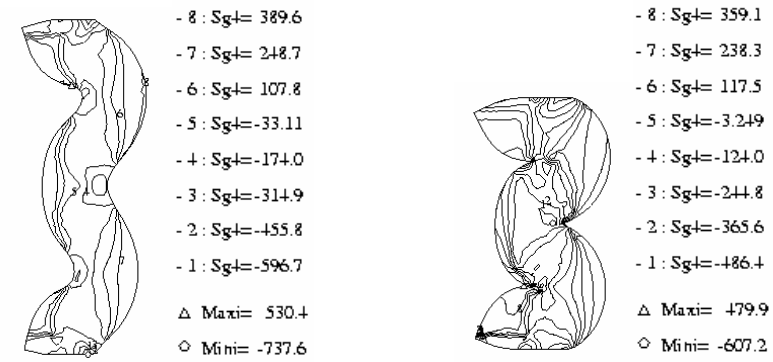

(k) Stress $\sigma_{\theta\theta}$

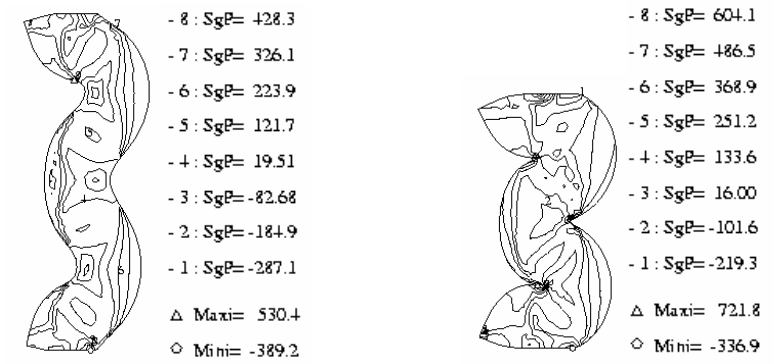

(l) Principal stress

(continue)

Figure 7: Predicted variation of nodal velocity, equivalent strain, different strain rates, and stresses at two stages (I) δ_1 =23.5 mm, and (II) δ_2 = 30 mm compression (specimen A254).

(continued)

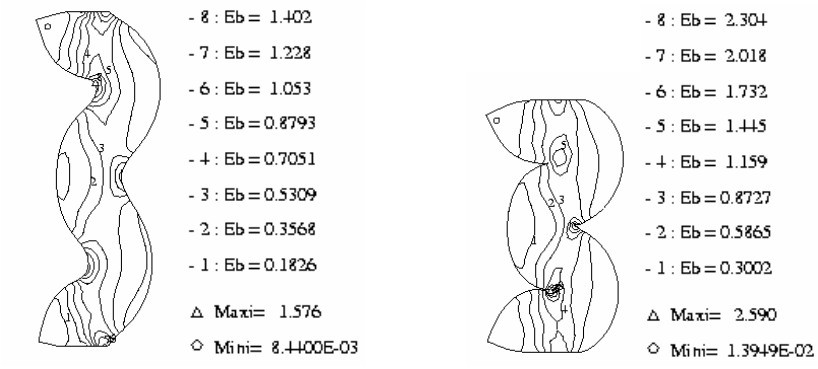

(m) Equivalent strain $\bar{\varepsilon}$

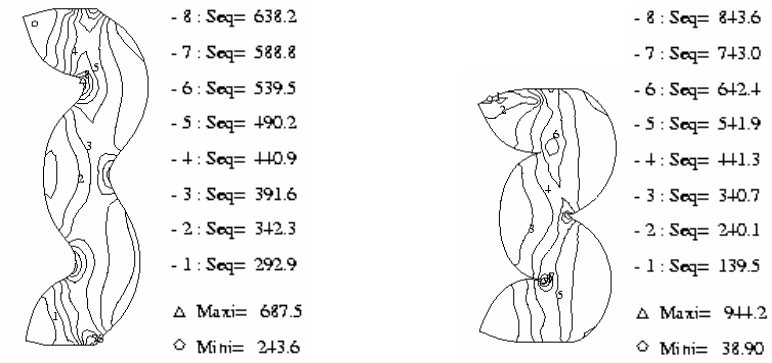

(n) Equivalent strain $\bar{\sigma}$

Figure 7: Predicted variation of nodal velocity, equivalent strain, different strain rates, and stresses at two stages (I) δ_1 =23.5 mm, and (II) δ_2 = 30 mm compression (specimen A254).

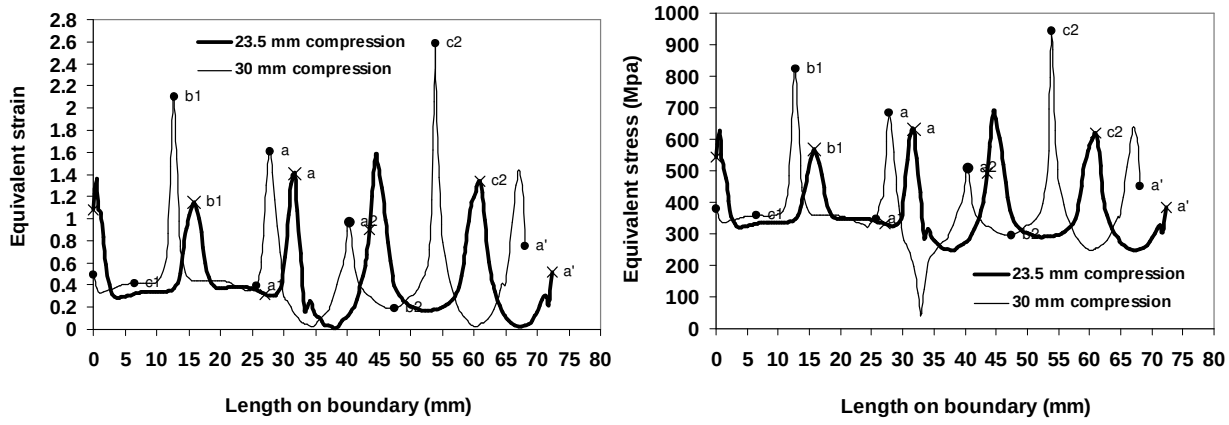

(a) (b)

Figure 8: Variations of (a) equivalent strain and (b) equivalent stress on boundary of tube at 23.5 mm and 30 mm compression (specimen A254).

mm compression. Variation of the ε_{zz} is quite similar with the variation of $\bar{\varepsilon}$. Variations of the hoop strain $\varepsilon_{\theta\theta}$ at points a2, b2, c2 are similar to the variations of the $\bar{\varepsilon}$ but at points a1, b1, c1 are quite different. After comparing the variations of $\bar{\varepsilon}$, ε_{zz} and $\varepsilon_{\theta\theta}$ at all these points it is clear that at point a1 major strain is developed due to the hoop stretching while b1 is the point where major strain develops due to direct compression. The strains at points a2 and c2 are due to combined effect of the compression, hoop tension and bending.

To further peep inside the compression process the variation of the normal stress and shear stress on the lines a2a1, b2b1 and c2c1 after 23.5 mm compression were investigated and these are shown in Fig. 10. The magnitude of shear stress on all these three lines is very small as compared to the magnitude of the normal stress. Variation of the normal stress on line b2b1 is exactly opposite of the variation on lines a2a1 and c2c1 due to their opposite curvature. Magnitude of the positive normal stress is very high as compared to the negative normal stress and also it occurs on a longer portion of the length of a2a1, b2b1 and c2c1. This clearly shows that the tube deforms mainly due to axial compression with small hoop stretching and bending.

4.3 Effect of Friction on mode of collapse

The proposed simulation model has been also used to investigate the effect of the friction present between the tube-platen interfaces on the development of axisymmetric multiple barrelling mode of collapse. For this purpose a small simulation study was carried out on the tube specimen A254. In this total 10 sets having different values of α_1 and α_2 were used to perform the simulation study. Obtained mode of deformation at two stages after 23.5 mm and 30 mm compression in each case are presented in Fig. 11. Fig. 12 and Fig. 13 show the corresponding load-compression and energy-compression curves for different sets of the α_1 and α_2. After observing the figures

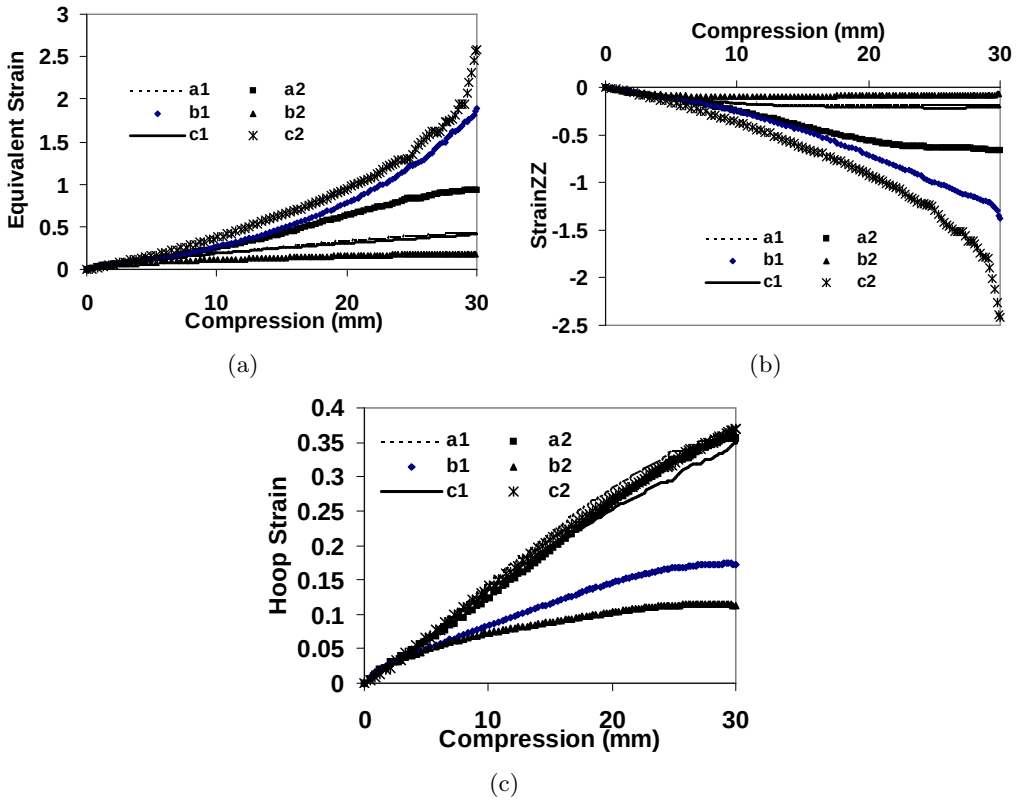

Figure 9: Variation of strains (a)$\bar{\varepsilon}$, (b)ε_{zz} and (c) $\varepsilon_{\theta\theta}$ at six key points a1, a2, b1, b2, c1 and c2 with compression (specimen A254).

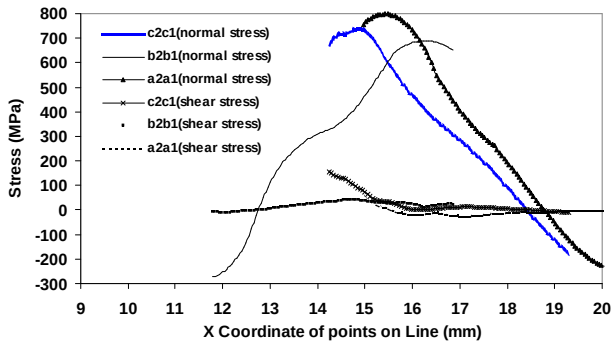

Figure 10: Variation of normal stress and shear stress on line a2a1, b2b1 and c2c1 at 23.5 mm compression (specimen A254).

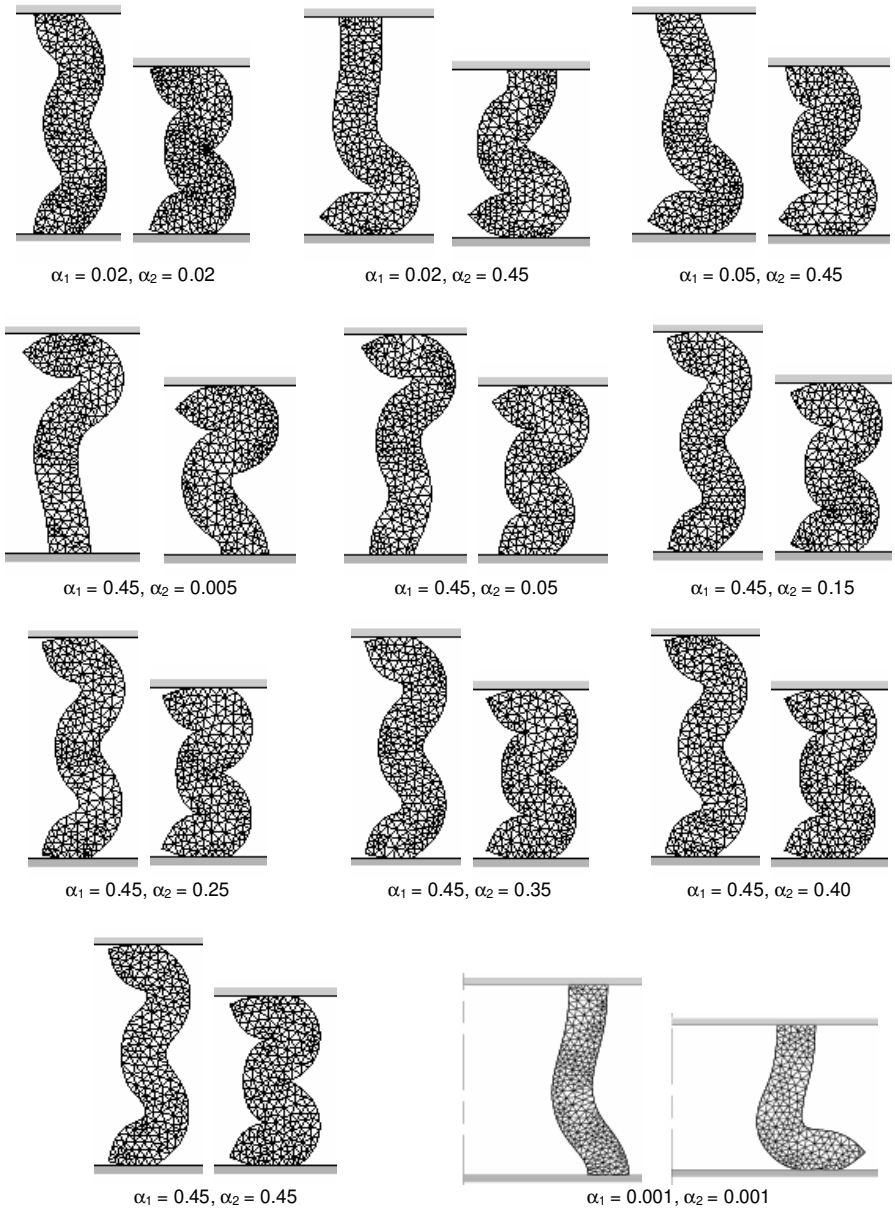

Figure 11: Computed deformed shapes at two main stages ($\delta_1 = 23.5$ mm, $\delta_2 = 30$ mm) of the development of axisymmetric multiple barrelling mode of collapse for specimen A254 for different values of coefficient of friction.

12 and 13 one can conclude that the friction present between the tube-platen interface does not change the energy absorbing capacity of the tube appreciably. On the otherhand the mode of deformation is highly dependent on the relative value of the α_1 and α_2. If α_1 is very higher as compared to the α_2 then the bulging of the tube would start from the α_1 side and viceversa. If the value of the α_1 and α_2 are very small which is not practically possible then the mode of deformation will not be axisymmetric multiple barrelling (see Fig. 11 $\alpha_1 = 0.001$, $\alpha_2.= 0.001$ and Fig. 12). Fig. 14 presents the energy absorbed in friction for different sets of the α_1 and α_2. After comparing Fig. 13 and Fig. 14 it is clear that the enrgy absorbed in friction present between the tube-platen interfaces is very small as compared to the total energy absorbed by the tube in development of the axisymmetric multiple barrelling mode of collapse.

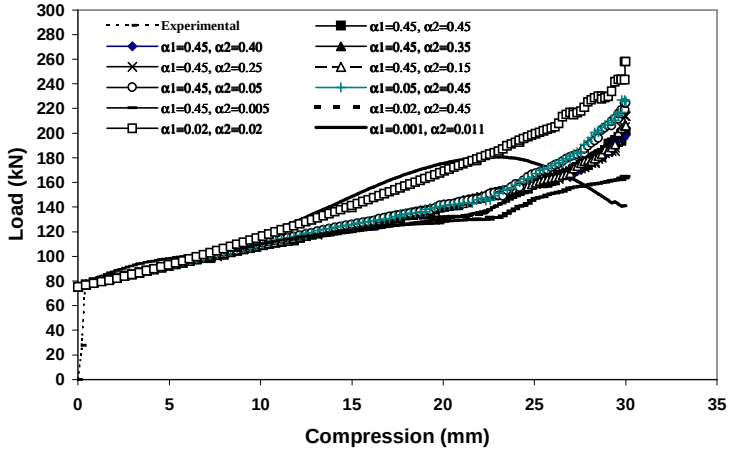

Figure 12: Comparison of load-compression curves for different sets of α_1 and α_2 for Axisymmetric multiple barrelling mode of collapse (specimen A254).

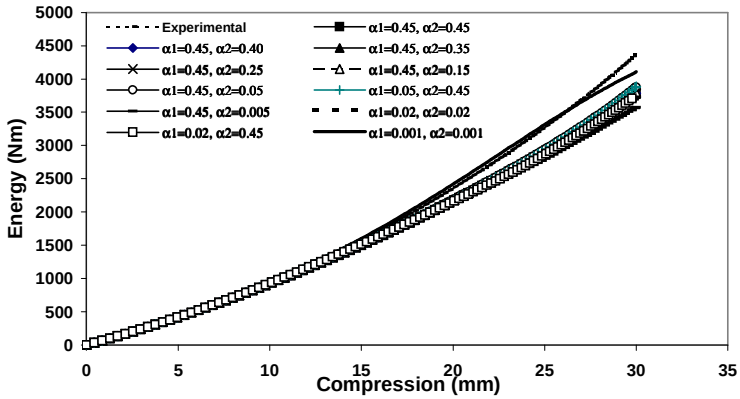

Figure 13: Comparison of energy-compression curves for different sets of α_1 and α_2 for Axisymmetric multiple barrelling mode of collapse (specimen A254).

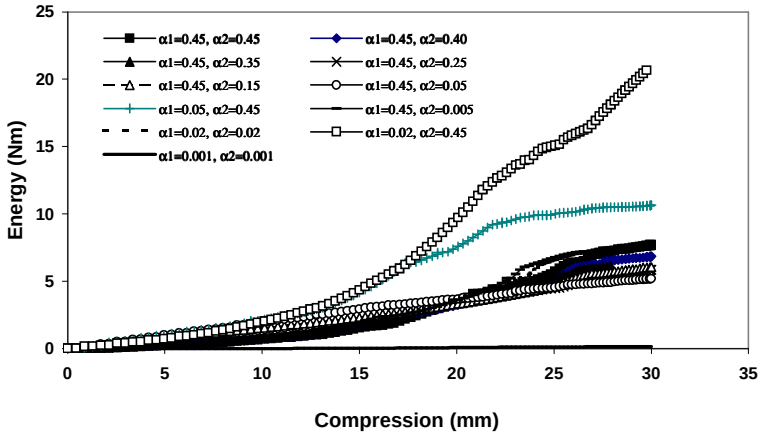

Figure 14: Variation of absorbed energy in friction with compression for different sets of α_1 and α_2 for Axisymmetric multiple barrelling mode of collapse (specimen A254).

5 Conclusions

An experimental investigation of the axial compression of thin and thick aluminium round tubes (D/h ratio between 7 and 38) between two flat platens is presented. Tubes having D/h ratio less than approximately 8 were deformed in axisymmetric multiple barrelling while others in axisymmetric concertina mode of collapse. Nonlinear FE model of development of axisymmetric multiple barrelling mode of collapse is also presented. Presented model was validated by comparing experimental and computational results on load-compression and energy-compression curves and deformed shapes of the tubes at various stages of deformation. Variations of different components of strain rates, stresses and strains are presented to help in predicting the mode of collapse. During the development of the axisymmetric multiple barrelling mode of collapse almost whole tube deforms throughout the compression process. Only a very small part of the tube remains undeformed. The deformation in the tube occurs mainly due to direct axial compression associated with hoop stretching and bending.

A numerical study was also carried out to investigate the effect of friction present between the tube-platen interfaces on the axisymmetric multiple barrelling mode of collapse. Friction present between the tube-platen interface has negligible effect on the energy absorbing capacity of the axisymmetric multiple barrelling mode of collapse. On the otherhand this friction to a great extent affects the mode of deformation.

References

[1] K. J. Bathe, J. Walczak, O. Guillermin, P. A. Bouzinov, and H. Y. Chen. Advances in crush analysis. *Computers and Structures*, 72:31–47, 1999.

[2] Arthur A. Ezra and R. J. Fay. An assessment of energy absorbing devices for prospective use in aircraft impact situations. n. proceeding of a symposium held at stanford university california june 28 & 29. In G. Hormone and N. Perron, editors, *Dynamic response of structures*, pages 225–246, 1972.

[3] FORGE2. *Finite element analysis code for metal forming problems Version 2.5*. Cemef, Sofia Antipolis, France, 1992.

[4] N. K. Gupta, G. S. Sekhon, and P. K. Gupta. A study of fold formation in axisymmetric axial collapse of round tubes. *International Journal of Impact Engineering*, 27:87–117, 2001.

[5] N. K. Gupta and R. Velmurugan. Consideration of internal folding and non-symmetric fold formation in axi-symmetric axial collapse of round tubes. *Int. J. Solids Structures*, 34:2611–2630, 1997.

[6] N. J. Hoff. Approximate analysis of structures in presence of moderately large creep deformations. *Q. Appl. Math.*, 12, 1954.

[7] W. Johnson and S. R. Reid. Metallic energy dissipating systems. *Applied Mechanics Review*, 31(3):277–288, 1978.

[8] L. P. Mikkelsen. A numerical axi-symmetric collapse analysis of visco-plastic cylindrical shells under axial compression. *Int. J. of Solids and Structures*, 36:643–668, 1999.